Monthly Notices of the ROYAL ASTRONOMICAL SOCIETY

MNRAS **522,** 5775–5787 (2023) https://doi.org/10.1093/mnras/stad1261
Advance Access publication 2023 April 27

Rotational state-changes in C_5N^- by collisions with He and H_2

R. Biswas,[1] K. Giri,[2] L. González-Sánchez,[3]★ F. A. Gianturco,[4]★ U. Lourderaj,[1] N. Sathyamurthy,[5]★ A. Veselinova,[3] E. Yurtsever[6] and R. Wester[4]

[1]*School of Chemical Sciences, National Institute of Science Education and Research (NISER) Bhubaneswar, An OCC of Homi Bhabha National Institute, Khurda, Odisha, 752050, India*
[2]*Department of Computational Sciences, Central University of Punjab, Bathinda 151401, India*
[3]*Departamento de Química Física, University of Salamanca, Plaza de los Caídos sn, E-37008 Salamanca, Spain*
[4]*Institut für Ionenphysik und Angewandte Physik, Universität Innsbruck, A-6020 Innsbruck, Austria*
[5]*Indian Institute of Science Education and Research Mohali, SAS Nagar 140306, India*
[6]*Department of Chemistry, Koc University Rumelifeneriyolu, TR 34450 Istanbul, Turkey*

Accepted 2023 April 25. Received 2023 April 25; in original form 2023 January 10

ABSTRACT

The anion C_5N^- is one of the largest linear (C,N)-bearing chains detected in the interstellar medium. Here we present and discuss the general features of new ab initio potential energy surfaces describing the interaction of this linear anion with He and H_2. We employ a Legendre Polynomials expansion representation for the former and an artificial neural network fit for the latter. We then carry out quantum scattering calculations to yield rotationally inelastic cross-sections for collisions with He and H_2, using relative translational energy values in the range of 0.1–300 cm^{-1}. We then obtained the corresponding inelastic rate coefficients as a function of temperature covering the range from 1 to 100 K. The results for these two systems are compared with each other, as well as with the earlier results on the C_3N^- colliding with the same partners. We found that the final inelastic rate coefficients for this anion are all fairly large, those from collisions with H_2 being the largest. The consequences of such findings on their non-equilibrium rotational populations in interstellar environments are discussed in our conclusions.

Key words: astrochemistry – molecular data – molecular processes – methods: numerical – ISM: molecules – photodissociation region (PDR).

1 INTRODUCTION

In recent years, several linear C-bearing and (C,N)-bearing chains of molecular anions have been detected at various sites in the interstellar media (ISM), specifically CN^-(Agúndez et al. (2010), C_3N^- (Thaddeus et al. 2008), C_5N^- (Cernicharo et al. 2008), C_4H^- (Cernicharo et al. 2007; Agúndez et al. 2008), C_6H^- (McCarthy et al. 2006), and C_8H^- (Brünken et al. 2007; Remijan et al. 2007). Those reported so far constitute different terms of the general linear chains associated with the polyynes and cyanopolyynes species. Astrophysical detection relies heavily on the spectroscopic investigations of such species in the laboratory and on matching sighted lines with those observed in the lab. Additionally, in order to carry out astrophysical modelling of population evolution of their distributions over a variety of internal states, important indicators are provided by the rate coefficients for the probability of rotational state-changes induced by their interaction with He and H_2, both partners present in substantial amounts in the ISM. The collision-induced occurrence of non-LTE (local thermal equilibrium) population for rotational states in molecular partners could, in fact, be a significant path to further radiative emission from different excited spectral lines in the observational microwave regions. Measurement of these rate coefficients in the laboratory is still challenging, while the available quantum mechanical methods can be used to compute them and then enter their results within networks of kinetic modelling of the underlying chemistry. Botschwina and Oswald (2008) had computationally determined the structural characteristics of some of these species to help observational sighting in the ISM or in the laboratory. In particular, they found that the vibrational frequencies for C_5N^- range from 2235.5 to 96.5 cm^{-1}. Since the focus of our work is on rotational inelastic transitions in C_5N^-, and also at low energies (E_{trans} = 0.1–100 cm^{-1}, the latter being the range of the relative collision energies), it can be safely assumed that their vibrational modes would hardly play any role at the energy regimes we are considering in our present study.

The chemistry of formation of such cyanopolyyne chains has also been the object of several studies and speculations (e.g. see Cernicharo et al. 2020).The possible formation of anions from the neutral radical via a Radiative Electron Attachment (REA) process has been considered in some detail (as quoted in Jerosimić, Gianturco & Wester 2018), while a more direct chemical route by reaction of the HC_5N with H^- has also been put forward by our group (Satta et al. 2015), since our calculated rates were found to be large enough to be relevant within the chemical network producing these anions. In the final analysis, however, the various options indicated by the current literature have not yet coalesced into a unique proof of the chemical formation of the title anion.

Rotational excitation and de-excitation in CN^-, the smallest term of the cyano-chain series, in collision with He and H_2 were investigated by Kłos and Lique (2011) and by some of the present

★ E-mail: Francesco.Gianturco@uibk.ac.at (FG); nsathyamurthy@gmail.com (NS); lgonsan@usal.es (LS)

authors (González-Sánchez et al. 2020). Similar studies have been carried out for the C_3N^-–He and C_3N^-–H_2 systems, by Lara-Moreno et al. (2017b, 2019b). On the other hand, there has been no study reported on the collision-induced excitation/de-excitation of C_5N^- rotational states by He and H_2. This anionic system provides a greater computational challenge, given the longer length of its chain and the much higher density of its rotational states, as we shall further show below. The full treatment of all (roto-vibrational) degrees of freedom for C_5N^- interacting with He/H_2 is a very hard computational challenge; hence, this study shall focus first on considering the expected ISM conditions of such system, which should be in its ground vibrational modes and, at most, only rotationally excited, thereby restricting this study to a rigid rotor treatment of C_5N^-. This was also the approach in the earlier studies for CN^- and C_3N^- collisions with He and with H_2 (Lara-Moreno et al. 2017b, 2019b; González-Sánchez et al. 2020). The computed potential energy surfaces (PESs) are thus restricted to two and to four dimensions for C_5N^-–He and C_5N^-–H_2, respectively.

The ab initio PESs were computed at the CCSD(T)-F12b/aug-cc-pVTZ level of theory and corrected for basis set superposition error (BSSE). Extensive experience with such studies involving neutral rare gases as partners (e.g. see Feller, Peterson & Grant Hill 2010) has indicated that the above approach is essentially equivalent to using the coupled clusters singles doubles and perturbative triples (CCSD(T)) method up to the complete basis set (CBS) limit in order to describe the various minima of the anisotropic PESs. Extrapolation of F12b energies to the basis set limit was found to be very effective at reproducing the best standard method atomization energies. Even extrapolations based on the small cc-pVDZ-F12/cc-pVTZ-F12 combination proved capable of a mean absolute deviation of 0.20 kcal/mol. The accuracy and simultaneous cost savings of the F12b approach are such that it was shown to enable high-quality property calculations to be performed on chemical systems that are too large for standard CCSD(T). Additionally, the Long-Range (LR) regions of interaction were found to be reached correctly at the larger distances beyond about 20 Å, while our quantum dynamics, as will be discussed later, takes care of the asymptotic regions by correctly extrapolating the multipolar coefficients using their analytic representation during the propagation of the scattering solutions (see below).

The well-known Legendre Polynomial expansion into multipolar coefficients was generated from the ab initio PES for the C_5N^-–He system. For the C_5N^-–H_2 case, the artificial neural network (ANN) method has been used to directly fit the raw points of the ab initio PES in four dimensions. The methods we have adopted, and the results we have obtained, are presented and discussed in detail in the following Sections.

2 COMPUTATIONAL METHODS

2.1 The computed potential energy surfaces

The geometry of the C_5N^- anion was optimized using the cc-pVQZ basis set via the MOLPRO suite of computer programmes (Werner et al. 2012). Its ground state was found to be a linear chain with the following bond distances: $C_1-C_2 = 1.261\,93$ Å, $C_2-C_3 = 1.349\,53$ Å, $C_3-C_4 = 1.234\,81$ Å, $C_4-C_5 = 1.361\,88$ Å, and C_5–N = 1.172 54 Å, making the overall length of the chain, treated as a rigid rotor, to be 6.380 69 Å. These features are in good agreement with the previous study by the Botschwina's group (Botschwina & Oswald 2008). The C_5N^-–He interaction potential was computed using the basis set expansion already mentioned earlier. It was obtained as a function of R, the radial separation between the He

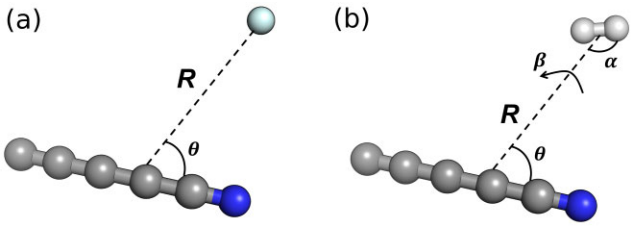

Figure 1. Illustration of (panel a) the polar coordinates (R, θ) used for the C_5N^-–He system and (b) the four variables (R, θ, α, and β) used for the C_5N^-–H_2 system. The N− atom of the chain is indicated in blue.

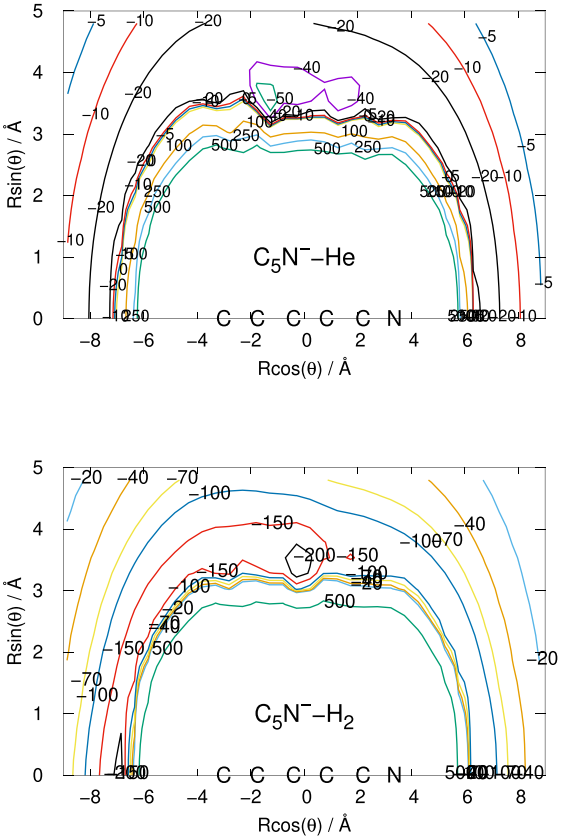

Figure 2. Potential energy contours for the C_5N^-–He system (upper panel) and the C_5N^-–H_2 system (lower panel). The latter is given by the arithmetic average of 21 combinations of the α and β angles.

atom and the centre of mass of the rigid rotor, and of the polar angle (θ) between R and the linear rigid rotor as illustrated in Fig. 1(a). Here $\theta = 0^\circ$ corresponds to the He atom approaching the N− end of the polyatomic molecular anion while $\theta = 180^\circ$ indicates the approach to its C− end.

The anisotropy of the potential for the C_5N^-–He system is evident from the potential energy contours, given as a function of R and θ by the isolines on the upper panel of Fig. 2. We also see there that the deepest attractive well region is for the T-shaped geometry centred on the mid C-atom of the chain. This is what should be expected from the closed-shell nature of the neutral He that tends to avoid the negative charge at the C-end of the anion. Hence, the potential has a minimum of -60 cm^{-1} at $R = 3.5$ Å and $\theta = 100^\circ$ indicating the T-shaped geometry to be the global minimum configuration for this system. In generating the initial raw points, the θ steps were of

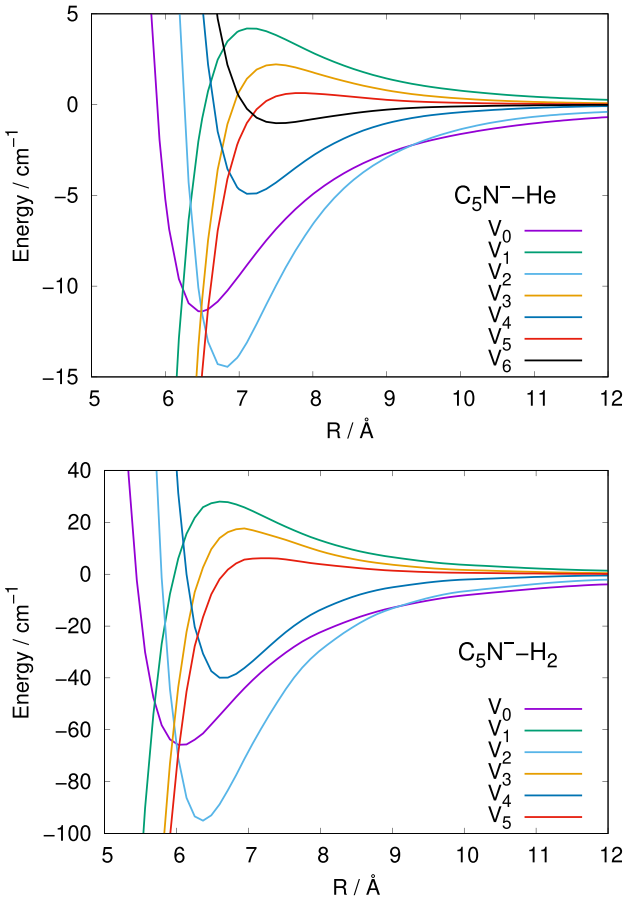

Figure 3. Plot of the Legendre coefficients as a function of R for the two systems C_5N^- - He (upper panel) and C_5N^- - H_2 (lower panel). The latter data originate from the arithmetic average of 21 combinations of α and β angles.

10°, while the values of the radial parameter R, depending on the angular value, were varied from 1.8 to 8.0 Å with increments of 0.1 Å. Additionally, we used the more distant radial values of 9, 10, 12, 15, 20, and 25 Å at all angles.

For the case of the He partner, the final PES was expanded in orthogonal Legendre polynomials for the angle θ:

$$V(R,\theta) = \sum V_\lambda(R) P_\lambda(\cos\theta). \quad (1)$$

The number of λ terms that were required for numerical convergence was extended up to $\lambda = 80$, although at many of the collision energies sampled in our calculations, only 40 terms were sufficient. The strong angular anisotropy of the interaction potential for this system is confirmed when we examine a limited set of the radial expansion coefficients in the upper panel of Fig. 3. We see that such coefficients exhibit markedly different radial regions of coupling strength that depend on their λ label, and strongly affect the relative efficiency of state-to-state transitions as we shall further discuss in the following Section. This is because the λ value controls the direct coupling between rotational quantum states within the quantum dynamics (see below), hence can tell us about the different excitation probabilities for the involved state-changing processes.

For the case of the interaction with the rigid-rotor H_2,the full spatial potential was computed at the CCSD(T)-F12b/aug-cc-pVTZ level of theory and corrected for BSSE (Boys & Bernardi 1970). The

Table 1. The different data sets generated and used to perform the fitting of the initial PES points.

Data set	Description	Number of points
1	Original set	16 025
1a	Set 1 + 4000	20 000
2	Symmetry β	29 897
3	Set 2 + cubic splines	46 064
4	Set 3 + Boundary	58 448
5	Set 4 ($V < 2000$ cm^{-1})	52 734
6	Set 5 (w.o. boundary)	44 915

potential is a function of four independent variables R, θ, α, and β, where R is the centre-of-mass separation between the one of C_5N^- and that of H_2, θ is the polar angle around the centre of mass of C_5N^-, with $\theta = 0^o$ corresponding to the H_2 molecule approaching the N− end of the molecular anion and $\theta = 180^o$ corresponding to the approach at the C− end. α is the polar angle around the centre of mass of H_2, and β is the dihedral angle, as illustrated in Fig. 1(b). A total of 16 025 potential energy values were computed by varying θ systematically from 0 to 180° at intervals of 10°, α from 0 to 150° at intervals of 30° and β from 0 to 90° at intervals of 30°. The geometry with $\alpha = 180^o$ is identical to that with $\alpha = 0^o$. The homonuclear symmetry of H_2 requires that the potential for configurations with $\beta = X^o$ is the same as that for $\beta = (180-X)^o$. R was varied from 2 to 25 Å. All the computed V values are included in the supporting information.

An example of dimensionality-reduced potential energy contours, plotted in 2D polar coordinates for C_5N^- interacting with H_2 and given as an arithmetic average of 21 combinations of α and β, are reported in the lower panel of Fig. 2. The anisotropy of the interaction potential for this particular averaged geometry can be taken as a typical example for this system and is therefore given here for a qualitative discussion. It is easy to see in that figure, in fact, that the potential is now more attractive for H_2 than it was for He, the attraction being larger at the C− end than at the N− end and the well depth for C_5N^-–H_2 being three times larger than that for the C_5N^-–He case. For a pictorial comparison of the anisotropy of the two systems, the Legendre expansion coefficients for the H_2 partner (given from the arithmetic average of all 21 computed rotational angles) and for the He partner, are plotted in the two panels of Fig. 3.

The comparison of the radial coefficients reported by the two panels in that Fig. 3 shows very clearly that the overall coupling strength associated with the H_2 partner (lower panel) is markedly larger than the one produced by the He atom (upper panel). It is therefore to be expected that inelastic events would be more efficient for the former projectile than they would be for the latter. The results discussed in the following Sections will confirm this behaviour.

To generate a quantitative fit of the original raw points obtained in the case of C_5N^-–H_2, the ANN method (Raff et al. 2012; Sarkar & Bhattacharyya 2017; Biswas, Rashmi & Lourderaj 2020; Giri et al. 2022) was used. Its convergence required considerable amount of additional points to be provided as input over the range of the relevant variables. This additional data generation is reported in detail in Table 1. Hence, for a uniform distribution of points over the entire range of α and β, additional data points (around 4000 new points) were added to the initial ab initio set of values (see above). For $\alpha = 180^o$ and $\beta = \{30^o, 60^o, 90^o\}$, $V(\alpha = 0^o, \beta = 0^o)$, only the original energy values were used, while, to reflect the symmetry of the system, additional points along β were added by interpolation methods as described below. For example, the value of the potential

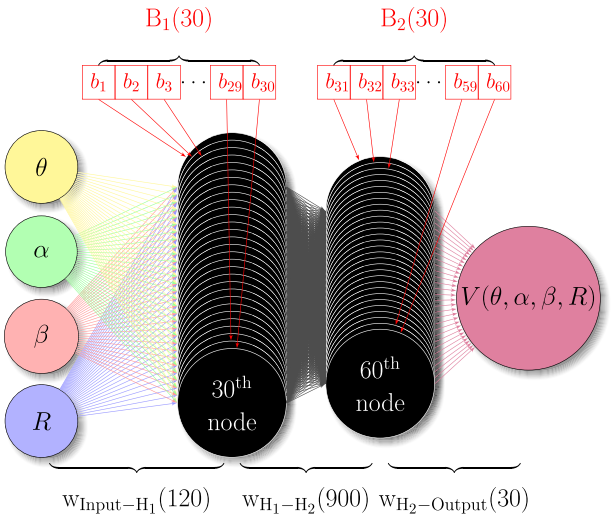

Figure 4. Neural network used to train the C_5N^-–H_2 PES. Weights are shown in black and biases in red. The numbers inside the parentheses are the corresponding number of parameters.

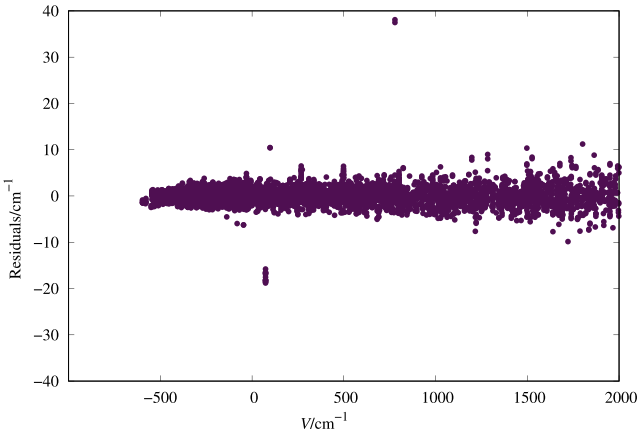

Figure 5. Plot of the residuals originating from the best ANN fit of the C_5N^-–H_2 original PES.

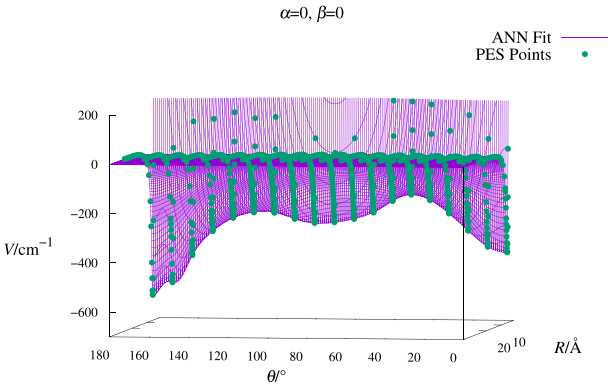

Figure 6. Plot of the PES obtained from the best ANN fit compared to the initial input points used to train the neural networks for $\alpha = 0^o$, $\beta = 0^o$.

for $\beta = 60^o$ is the same as that for the potential for $\beta = 120^o$. The initial distribution of ab initio raw points for R values > 10 Å was sparse and therefore this region was prone to overfitting. Hence, we used the one-dimensional cubic spline method (Sathyamurthy & Raff 1975) to interpolate the initial V values, so that we could add in this way an additional 15 000 points. Furthermore, we added data points beyond the natural limit of θ to ensure that the ANN fit behaved smoothly in the range $\theta = 0^o$–180^o. For example, we added $V(\theta = 200^o)$ which is equal to $V(\theta = 160^o)$, and other extra points were obtained in a similar manner.

The data Set 5 was used to fit the PES by employing the ANN method for potential energy values that were less than 2000 cm^{-1}. Set 6 was used to test the performance of the neural networks. For the transfer function we used a modified version of the logistic sigmoid function given by

$$\sigma(a) = \frac{2}{1 + e^{-2a}} - 1, \tag{2}$$

where a is the summation of all the inputs to any given node. The Bayesian regularization (MacKay 1992) optimizer was used to train the network as implemented in MATLAB (MATLAB 2018). The final fit was converted into a C++ code using the MATLAB coder and was further converted into a FORTRAN routine. The asymptotically correct long-range potential with a switching function was also added to the FORTRAN code (as described below). A copy of the FORTRAN code is included in the Supplementary Information.

Initially, we used a shallow neural network consisting of 300 neurons in one layer. The best fit we obtained had a root mean square deviation (RMSD) of 9.27 cm^{-1} with the maximum error of 176 cm^{-1} for $V = 1966.88$ cm^{-1} at $R = 5.1$ Å, $\theta = 160^o$, $\alpha = 150^o$, and $\beta = 90^o$. To further improve the fit, we used a neural network consisting of two hidden layers (H_1 and H_2) and varied the number of nodes in each hidden layer. Fig. 4 shows the schematics of the network employed in this study.

We must add that we used 100 per cent of the available data to train the network. By changing the initial choice of weights and biases for each node, and by optimizing the number of epochs (training cycles), we could obtain the best fit that had an RMSD of 0.87 cm^{-1}, with the largest error being 38 cm^{-1} when $V = 778$ cm^{-1}. This was accomplished by using 30 neurons in each hidden layer. The present optimization was performed with respect to mean square error (MSE) as given in the algorithm used by MATLAB.

The residual plot for the best fit is given in Fig. 5. The quality of the fit is illustrated in the PES plotted in (R, θ) space in Fig. 6 for $\alpha = 0^o$, $\beta = 0^o$.

The computed ab initio PES and the ANN fit are restricted to a finite range of R. The ANN fit is connected smoothly to the asymptotically correct long-range potential using a switching function as described below.

The long range potential is given by

$$V_{LR}(\theta) = -\frac{\alpha_0}{2R^4} + \frac{2\alpha_0\mu}{R^5}\cos(\theta), \tag{3}$$

where $\alpha_0 = (\alpha_\parallel + 2\alpha_\perp)/3$. Using the results of $\alpha_\parallel = 6.38049$ au and $\alpha_\perp = 4.57769$ au for $r = 1.4$ au (0.7408 Å) of H_2 reported by Kolos and Wolniewiez (1967), $\alpha_0 = 5.1786$ au. And the rigid-rotor dipole moment of C_5N^- is $\mu = 3.31370$ au.

The final form of the potential using the switching function is given by

$$V_f = f_s V_{ANN} + (1 - f_s)V_{LR}, \tag{4}$$

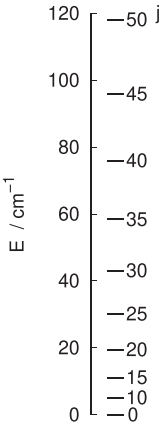

Figure 7. An illustrated energy ladder of the rotational energy levels of C_5N^- involved within an energy range of 120 cm^{-1}.

where the switching function is

$$f_s(R) = \frac{1}{e^{\frac{(R-R_0)}{\Delta R}}+1}, \tag{5}$$

and $R_0 = 22$ and $\Delta R = 0.5$ Å.

2.2 Treatment of the quantum dynamics

Since C_5N^- has a fairly small rotational constant (B_e) of 0.046 33 cm^{-1}, even at the lowest collision energies it is necessary to couple within the quantum dynamics a rather large number of rotational states to converge the Coupled Channel expansion, as further discussed below. A schematic view of the energy ladder is reported in Fig. 7, clearly showing how dense is the number of states per unit of energy. It therefore follows that to carry out exact Coupled Channels (CC) calculations (Green 1975) for the (C_5N^-/H_2) system would be computationally highly time-consuming. Therefore, we decided to carry out instead Helicity Decoupled (HD) quantum scattering calculations for this system (Kouri 1975). To be able to compare the results for the two systems under study, we have used the HD approximation also for the simpler case of the C_5N^-/He system. We shall further show below that the HD calculations were found to be, for this system, very close to the exact CC calculations.

The time-independent Schrödinger equation for collision between two rigid rotors, formulated in a space-fixed frame and also in the equivalent body-fixed frame, has been discussed in detail by Green (1975). While the CC calculation uses the space-fixed frame, the HD approximation uses the rotating body-fixed frame in which the projection quantum number (K) for the rotational angular momentum ($\mathbf{j}$) of the individual rotor (or the collective $\mathbf{j}_{12}$ in the case of two rotors) is taken to be with respect to the interparticle axis R. While the interaction matrix is diagonal in K, the $\mathbf{L}^2$ (= $(\mathbf{J}-\mathbf{j})^2$ operator, where $\mathbf{J}$ is the total angular momentum) is non-diagonal in K. The HD approximation neglects the off-diagonal matrix elements in K, but evaluates the diagonal matrix elements exactly, as given in the following equation :

$$\langle jKJ|L^2|jKJ\rangle = J(J+1) + j(j+1) - 2K^2. \tag{6}$$

It is important to point out that in this approximation only basis functions with $K \leq j$ are included in the expansion set. For a detailed discussion on decoupling angular momenta in molecular collisions, the reader is referred to the work of Kouri (1975). For an example of a successful use of the HD approximation for a tri-atom system, the reader is also referred to our earlier work of Buonomo et al. (1997).

We have computed the rotational inelastic cross-section (σ) values for a range of relative translational energy (E_{trans}) and the rate coefficient (k) values for a range of temperatures between $T = 1$ and 100 K. It turns out that the range of E_{trans} and T investigated allows us to make a significant comparison of our computed results with the results reported earlier (Lara-Moreno et al. 2017b, 2019b) for a similar, but smaller, molecular ion: C_3N^-. We remind the reader that our present definition of E_{trans} corresponds to relative kinetic energy between partners without reference to the internal energy content of the molecular species. It is therefore the collision energy of the scattering process. This definition is further repeated for clarity after the equation (7) discussed later on.

We further find that, in practice, the presently obtained results can be reliably extrapolated to higher temperatures, although for a safer comparison, we also carried out the scattering calculations for both systems up to 300 cm^{-1}, thus allowing us to obtain converged rate coefficients up to 100 K (see the discussion below). The inelastic rate coefficients $k_{j\rightarrow j'}(T)$ were obtained using the standard numerical integration procedure as the convolution of the cross-sections over a Boltzmann distribution of the relative translational energies, E_{trans}

$$k_{j\rightarrow j'}(T) = \left(\frac{8}{\pi\mu k_B^3 T^3}\right)^{1/2} \times \int_0^\infty \sigma_{j\rightarrow j'}(E_{trans}) E_{trans}\, e^{-E_{trans}/k_B T}\, dE_{trans}, \tag{7}$$

where E_{trans} has been mentioned earlier and corresponds to the relative collision energy of the partners.The numerical integration was checked for the convergence of the final rate coefficient values at different points of the required range of temperatures.

For $C_5N^-(j_1)$–He collisions, the HD calculations were carried out for the initial rotational states $j_1 = 0$ and 5 using the MOLSCAT (Hutson & Sueur 2019a,b) computer code.

Since the working of the MOLSCAT code and the theory behind it have been already extensively described in the literature (Hutson & Sueur 2019a,b), we only mention here the parameters used in the current study. For the case of the He partner interacting with the present molecular anion we employed the following data: JTOTL = 0, JTOTU = 50–240 depending upon E_{trans}, BE = 0.046 292, JMAX = 10–50 depending upon E_{trans}, LMAX = 40–80 also depending upon E_{trans}. RMAX was taken to be as large as 220 Å for the lower energy (E_{trans} = 0.1 cm^{-1}) collisions and it was lowered to a value of 50 Å for the higher energies. We remind the reader once more that our inelastic cross-sections were generated up to collision energy values of 300 cm^{-1}.

In the calculations of the inelastic cross-sections for C_5N^-–H_2, we also employed the MOLSCAT code, using the ANN-fit of the interaction potential further expanding the latter in terms of a product of two Legendre polynomials (Hutson & Sueur 2019a,b):

$$V(R,\theta,\alpha,\beta) = \sum_{\lambda_1,\lambda_2,\lambda} V_{\lambda_1,\lambda_2,\lambda}(R) \sum_{\mu} \langle \lambda_1, \mu, \lambda_2, -\mu|\lambda, 0\rangle \left(\frac{2\lambda+1}{4\pi}\right)^{1/2} \times Y_{\lambda_1}^{\mu}(\theta,\phi_1) Y_{\lambda_2}^{-\mu}(\alpha,\phi_2) \tag{8}$$

where $Y_{\lambda_1}^{\mu}(\theta,\phi_1)$ and $Y_{\lambda_2}^{-\mu}(\alpha,\phi_2)$ refer to the spherical harmonics in (θ, ϕ_1) and (α, ϕ_2). In this specific notation, the final potential now depends only on $\beta = \phi_1 - \phi_2$. Some of the leading terms in the

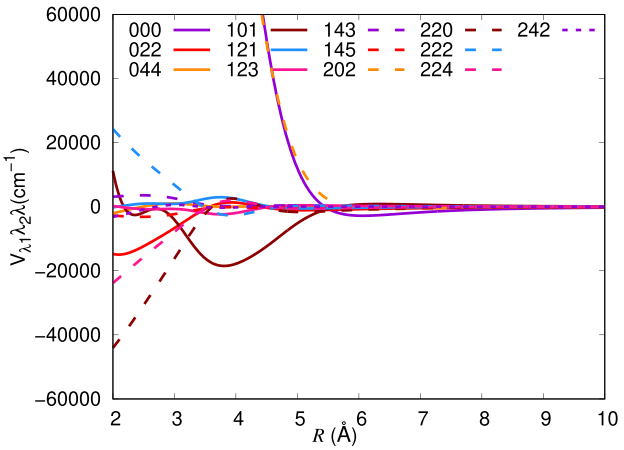

Figure 8. Computed multipolar expansion coefficients as a function of R, obtained from the MOLSCAT code using the present ANN fit of the ab initio PES for the (C_5N^-–H_2) system.

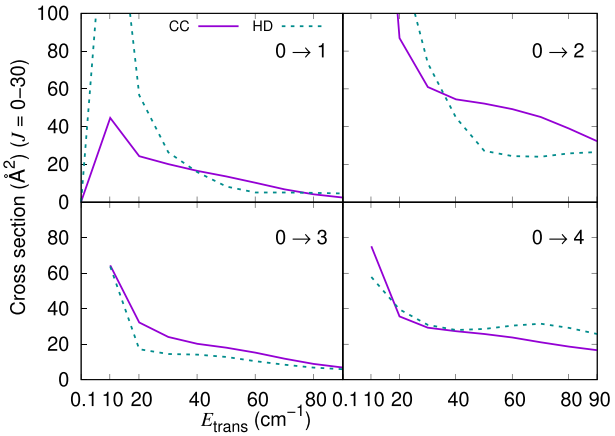

Figure 9. Comparing excitation cross-sections as a function of E_{trans} for $j_1 = 0 \rightarrow j_1' = 1$, 2, 3, and 4 transitions in C_5N^- in collision with He. The colour code indicates with the solid purple lines the exact CC calculations and with the blue dashed lines the HD calculations. See the main text for further details.

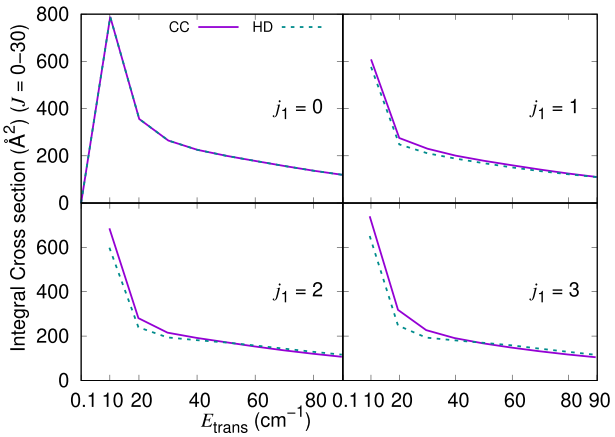

Figure 10. Comparing total excitation cross-sections for $j_1 = 0,1,2,3 \rightarrow$ all $j_1' > j_1$ for C_5N^- in collision with He. The solid purple lines indicate the exact CC calculations, while the blue dashed lines the HD calculations. The highest j_1' value changes depending on the collision energy and varies from 14 to 43. See the main text for further details.

expansion obtained by the MOLSCAT code are plotted as a function of R in Fig. 8.

Note that the second index (λ_2) in the expansion coefficients remains even because of the homonuclear symmetry of the collision partner H_2. Furthermore, due to the shallow well and the large anisotropy of the system, no single term in the expansion dominates in terms of its coupling strength (in contrast to what was found earlier by us for the cation-neutral system of HeH^+–H_2 (Giri et al. 2022). One should also note that the smoothness of the curves depicting the variation of the expansion coefficients along the radial variable R testifies to the quality of the ANN-fit we have obtained here. In the short-range radial regions of the coefficients reported by Fig. 8 we observe several oscillations in different radial coefficients. These are due to the strong orientational anisotropy of the PES and appear to compensate each other within different terms: we see, in fact, that oscillations in the $V_{2,2,2}(R)$ coefficient are compensated by out-of-phase oscillations in the $V_{2,2,0}(R)$ and $V_{2,2,4}(R)$ terms. Similarly, oscillations in the $V_{1,2,1}(R)$ coefficient are compensated by those in the $V_{1,2,3}(R)$ term. In other words, the cumulative effects coming from different terms will average out during the radial propagation and will therefore contribute very little to the final state-changing amplitudes of the asymptotic solutions.

Since the features of the MOLSCAT code, and the theory behind its functioning, are already described in great detail in the existing literature (Hutson & Sueur 2019a,b), we again mention only the working parameters used for this system: JTOTL = 0, JTOTU = 100–150 depending upon E_{trans}, BE = 0.04633, 60.8, J1MIN = 0, J1MAX = 6–150 depending upon E_{trans}, J2MIN = 0, J2MAX = 6, J2STEP = 2, L1MAX = 10, L2MAX = 4, IHOMO2 = 2, NPTS(1) = 21, NPTS(2) = 21, NPTS(3) = 25, for p-H_2 (j_2 = 0) as the collision partner. RMAX was taken to be as large as 220 for low-energy (E_{trans} = 0.1 cm^{-1}) collisions and it was lowered to a value of 60 for E_{trans} = 20–300 cm^{-1}.

3 RESULTS AND DISCUSSION

As reported in the previous Sections, we have employed for the quantum dynamics calculations a reduced angular momentum coupling scheme defined as the HD coupling method in our short overview. In order to test the quality of this choice, we have carried out exact CC calculations for the case of the He partner and compared them with the HD results. The data reported in the panels of the figures below indicate that the two dynamical approaches indeed yield results that are very similar with each other.

The results reported in Fig. 9 compare, over an extended energy range, the inelastic cross-sections from the ground rotational state of the anion to the $j_1' = 1$, 2, 3, and 4 excited levels. We clearly see that all these cross-sections are very similar, in magnitude and energy dependence, when either of the coupling schemes are used. The top left-hand panel data for the $j_1 = 0 \rightarrow j_1' = 1$ transition are the only data where a marked difference in size between CC and HD results is found, the differences occurring at collision energies near threshold where the HD results are larger by a factor of two. On the other hand, when we further look at the comparisons reported in the four panels of Fig. 10, we see that the excitation cross-sections summed up to the highest state accessible at the selected E_{trans} value are very similar to each other. The results for the HD (green dashed lines) and CC (solid purple lines) calculations are now nearly coincident in magnitude and energy dependence. Hence, this comparison indicates that the energy-

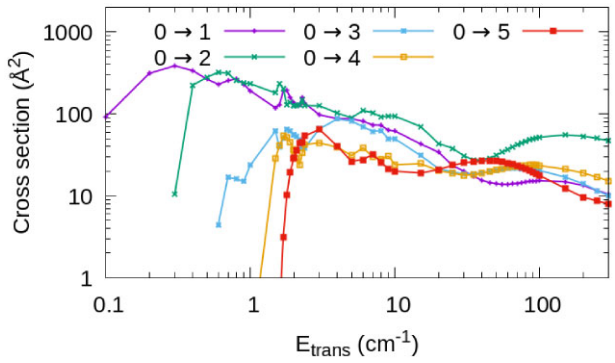

Figure 11. Excitation cross-section for $j_1 = 0 \rightarrow j_1' = 1$, 2, 3, 4, and 5 transitions in C_5N^- by collision with He. The data were obtained via HD quantum scattering calculations. See the main text for further details.

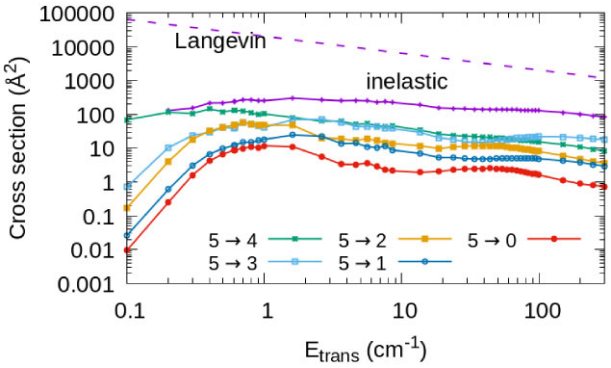

Figure 12. De-excitation cross-section for $j_1 = 5 \rightarrow j_1' = 0$, 1, 2, 3, and 4 transitions in C_5N^- in collision with He. Included in the plot is also the sum of the cross-section values for transition into all the different j_1' states, as well as the Langevin cross-sections given by the dashed line. Their calculation was done following equation (8).

transfer rate coefficients which we shall calculate in the following using the HD decoupling scheme are going to remain very close to the exact CC calculations. Only the single rate coefficients involving the state-to-state $j_1 = 0 \rightarrow j_1' = 1$ excitation at the lowest T values are, in fact, overestimated by the HD decoupling, although their effect on overall inelastic efficiency for the present system is completely compensated by the other transitions.

Given the similarity in coupling dynamics that we have found between collisions with He and those involving the $j_1 = 0$ hydrogen molecule, we can expect that the calculations for the latter system with the HD decoupling can also provide a fairly accurate descriptions of the corresponding inelastic rate coefficients, as we shall further discuss in the results reported below.

To be more specific, the cross-sections were evaluated for the He partner at $E_{\rm trans}$ (cm^{-1}): 0.1, 0.2, 0.3, 0.4, 0.5, 0.6, 0.7, 0.8, 0.9, 1.0, 1.488, 1.588, 1.688, 1.788, 1.888, 1.988, 2.0, 2.088, 2.188, 2.288, 2.388, 3.0, 4.0, 5.0, 6.0, 7.0, 8.0, 9.0, 10.0, 15.0, 20.0, 25.0, 30.0, 35.0, 40.0, 45.0, 50.0, 55.0, 60.0, 65.0, 70.0, 75.0, 80.0, 85.0, 90.0, 95.0, 100.0, and up to 300. They were employed in ranges [0.1–1] and [1.488–2.388] with step 0.1 [2–10] with step 1; [15–300] with step 5.

Our computed HD inelastic cross-sections ($\sigma_{j_1 j_1'}$) are plotted in Fig. 11 for the He projectile, starting at the $j_1 = 0$ and going to different values of j_1'. The threshold energy $2B_e = 0.092$ cm^{-1} for the $j_1 = 0 \rightarrow j_1' = 1$ transition is less than the lowest energy (0.1 cm^{-1}) shown along the x-axis. Energy thresholds of $6B_e$, $12B_e$, and $20B_e$ for the inelastic process resulting in $j_1' = 2$, 3, and 4 states, respectively, are visible in Fig. 11. The excitation cross-sections increase from threshold to a maximum value of about 400 Å^2 for $j_1' = 1$ and 2 and then decrease almost linearly (in the log-log scale) towards higher energies. There are noticeable oscillations in the excitation functions due to the occurrence of inelastic scattering resonances at low energies, coming from the presence of a significant potential well (~ 60 cm^{-1}) in the complex system. Since this study is focused on the inelastic rate coefficients which can be used in evolutionary models of the kinetics of the present anion, we have not pursued the analysis of the resonant feature in any detail.Furthermore, since no actual collision experiments on the cross-sections exist for the present system, we would not have any experimental comparison which could verify the accuracy of our resonance features.

Given the different coupling strengths between the lowest radial coefficients with (λ) values of 1 and 2, the cross-sections for the $j_1 = 0 \rightarrow j_1' = 2$ transition are slightly larger than that for the $j_1 = 0 \rightarrow j_1' = 1$, indicating that the direct rotational coupling of the two multipolar coefficients is fairly similar, as shown by the fact that, on the whole, these two inelastic cross-sections remain comparable in size and energy dependence over the examined range of energies. It is also clear from the figure that the inelastic cross-sections markedly decrease with an increase in the final j_1' to 3 and 4, especially at lower energies. This is linked to the fact that increase in the energy gaps between the involved levels induces smaller probabilities for energy transfer dynamics, a feature observed earlier for several other systems investigated in our group and seen, for example, in Giri et al. (2022).

De-excitation cross-sections for $j_1 = 5 \rightarrow j_1' = 4$, 3, 2, and 1, from collisions with He, are plotted in Fig. 12. It is worth pointing out once more that the cross-sections for the $\Delta j_1 = -1$ transition are larger than those for $\Delta j_1 = -2$ in the low range of energies, while becoming very similar in size at the higher energies. Similarly,at higher energies the cross-sections for $\Delta j_1 = -4$ are larger than those for $\Delta j_1 = -5$, a trend also shown when comparing with those for $\Delta j_1 = -3$. A similar behavior was observed by Lara-Moreno et al. (2017b, 2019b) in their study of de-excitation of C_3N^- ($j_1 = 5$) in collision with He and was attributed to the dominance of the even-labelled Legendre terms over the odd-labeled terms in the multipolar expansion of the potential, a feature also observed in our present system. The total de-excitation cross-sections ($\sum \sigma_{j_1=5\rightarrow 4,3,2,1,0}$), referred to as 'Inelastic', are also included in Fig. 12. The summed inelastic cross-section clearly decreases in size with an increase in $E_{\rm trans}$ beyond 10 cm^{-1}. This behaviour turns out to be in line with that found for the Langevin model (Lara-Moreno, Stoecklin & Halvick 2017a) of energy-transfer processes, which is also reported in the same figure. We also see in the comparison that the Langevin calculations markedly overestimate the actual values produced by the accurate quantum dynamics of this study. It is also well known that the excitation cross-sections can be computed from the de-excitation cross-sections, and vice-versa, using the principle of microscopic reversibility. We have checked that feature and indeed found that both methods produced the same results for this study. The cross-sections given by the Langevin model, $\sigma_{\rm L}$, are obtained from the following well-known expression:

$$\sigma_{\rm L} = \pi \left(\frac{2\alpha}{E_{\rm trans}} \right)^{1/2}. \quad (9)$$

where α is the polarisability of the neutral collision partner of that particular system. In our case, for the He atom, the value was taken to

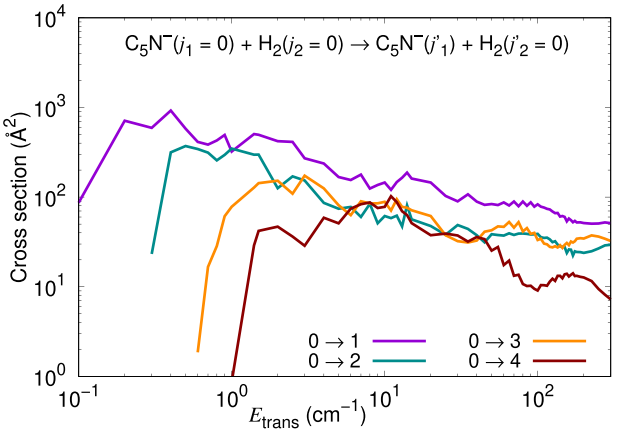

Figure 13. Excitation cross-section for $j_1 = 0 \rightarrow j_1' = 1$, 2, 3, and 4 transitions in C_5N^- by collision with para-H_2 ($j_2 = 0$).

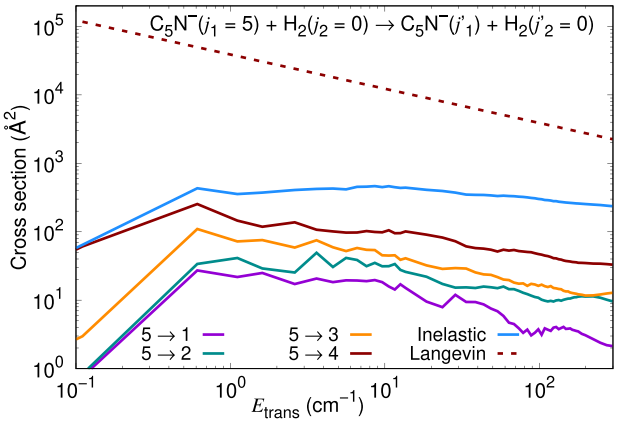

Figure 14. De-excitation cross-section for rotational transitions from $j_1 = 5$ to $j_1' = 4$, 3, 2, and 1 states of C_5N^- due to collision with para-H_2 ($j_2 = 0$). Included in the figure are the sum of cross-section values for transition into different states, labeled as Inelastic. The dashed line presents the cross-section values computed using the Langevin model, as given by equation (8).

be 0.208 Å^3, as already discussed in González-Sánchez et al. (2020), while for the H_2 collision partner, the value was 0.767 Å^3, as given by Kolos & Wolniewicz (1967).

For the case of H_2 ($j_2 = 0$) partner, the inelastic excitation cross-sections are plotted in Fig. 13 for different final j_1' values, starting from the initial state of $j_1 = 0$. As was noted earlier for the $C_5N^-(j_1 = 0)$–He system, the excitation cross-sections increase from threshold to a maximum value, which is here of the order of 1000 Å^2 for $j_1' = 1$ and 2 and then decrease almost linearly (in the log−log scale) towards higher energies. There are once more noticeable oscillations in the excitation functions, obviously due to the presence of inelastic scattering resonances originating from the presence of a significant potential well (~ 150 cm^{-1}) in the interaction between the two partners. As we have discussed previously for the He partner, we shall mainly focus on calculating inelastic rate coefficients since no detailed experiments exist on the cross-sections describing resonant features in these inelastic processes. It is also clear from the figure that the sizes of the cross-sections decrease with an increase in the final rotational state of the anionic partner to 2, 3, and 4, especially at lower energies, as seen earlier for the C_5N^-–He system. This is linked to the increase of the energy gaps between the involved states as Δj_1 increases and to the ensuing reduction of the dynamical probabilities for inelastic collisions when larger amounts of energy are being transferred.

The de-excitation cross-sections for $j_1 = 5 \rightarrow j_1' = 4$, 3, 2, and 1 transitions for C_5N^- in collision with para-H_2 ($j_2 = 0$) are plotted as a function of $E_{\rm trans}$ in Fig. 14. We see once again that the smaller energy gaps between the initial and the final states of the rotor yield larger cross-sections produced by quantum dynamics. The total de-excitation cross-section ($\sum \sigma_{j_1=5\rightarrow 4,3,2,1}$) values (referred to as 'Inelastic') are also included in Fig. 14. The summed inelastic cross-sections clearly decrease in size as a function of $E_{\rm trans}$, as it occurs with the Langevin model (Lara-Moreno et al. 2017a) reported in the same Fig. 14. As we had found for He, the correctly computed cross-sections are here orders of magnitude smaller than the qualitative data provided by the Langevin model.

Since the chief observables needed for astrophysical modelling are the rate coefficients (k), we have computed them for C_5N^- ($j_1 = 0$, 5, 10, 15)−He and H_2 ($j_2 = 0$) collisions and report them in the following Figs.

The results are presented in Fig. 15 for C_5N^- ($j_1 = 0$) with He, for different values of the transition index Δj_1. Here we see once more

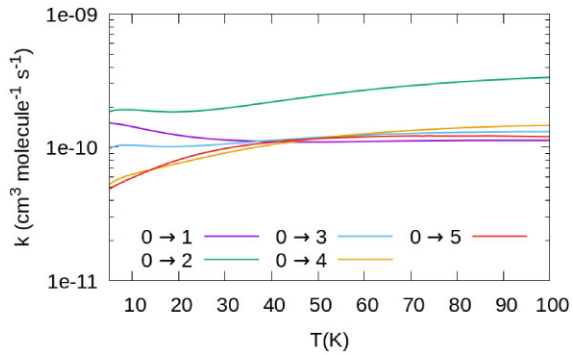

Figure 15. Excitation rate coefficient k for $j_1 = 0 \rightarrow j_1' = 1$, 2, 3, 4, and 5 transitions in C_5N^- by collision with He as a function of T.

that rate coefficients involving the $\Delta j_1 = 2$ process are significantly larger than those for the $\Delta j_1 = 1$, in keeping with the trend already observed for their excitation cross-sections in Fig. 11. Although rate coefficients for $\Delta j_1 = 3$, 4 and 5 are somewhat smaller, as the energy gaps increase with the increasing of the Δj_1, we see that beyond about 40 K, all the rate coefficients turn out to be very similar in size.

The rate coefficients for de-excitation processes from ($j_1 = 5$) involving He are plotted in Fig. 16 as a function of T. These data show that the $\Delta j_1 = -1$ rate coefficients are only slightly larger than those for the $\Delta j_1 = -2$, as was observed earlier by Lara-Moreno for the case of the C_3N^- ($j_1 = 5$)–He system. Additionally, we see that the values of the rate coefficients with $\Delta j_1 = -4$ transition are markedly larger than those for the $\Delta j_1 = -5$, which, in turn, are the smallest computed k values.

Fig.17 reports excitation rate coefficients from $j_1 = 0$ to $j_1' = 1$, 2, 3, 4, 5, and 6, for C_5N^- in collision with H_2 ($j_2 = 0$). These data show some interesting trends as a function of temperature: (i) the largest k values are for the $\Delta_{j_1} = +1$ transitions and are of the order of 5×10^{-10} cm^3 molecule^{-1} s^{-1} at $T = 1$ K. They then increase with increasing T, clearly in line with the behavior of the cross-sections discussed earlier; (ii) for larger Δj_1 transitions, there is a uniform increase in k with T, followed by a slight leveling-out with further increase in T. The initial trend is clearly a consequence

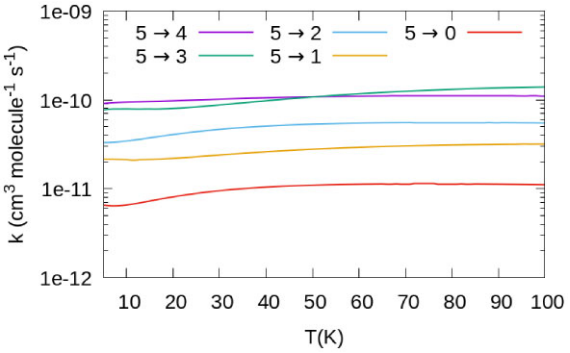

Figure 16. Computed rate coefficients as a function of T for the de-excitation from $j_1 = 5$ to different j_1' states of C_5N^- in collision with He.

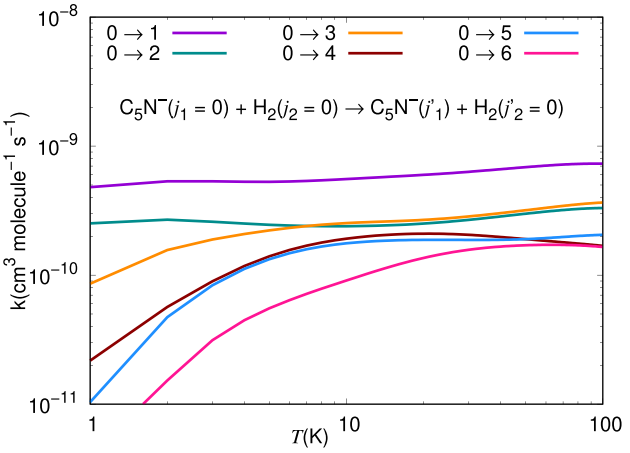

Figure 17. Excitation rate coefficients k for $j_1 = 0 \rightarrow j_1' = 1, 2, 3, 4, 5$ and 6 transitions in C_5N^- in collision with H_2 ($j_2 = 0$) as a function of T.

of the steep rise in the excitation function from the threshold, while the latter trend is due to a reduction at higher $E_{\rm trans}$ of the excitation cross-sections presented earlier. The general feature of obtaining smaller excitation rate coefficients as the energy gaps increase is fully confirmed by the data of Fig. 17.

The computed rate coefficients are plotted in Fig. 18 for the de-excitation processes from $j_1 = 5$, 10 and 15 down to a few lower states in each case, reported in the three panels of that Figure, starting from the top and going down to the bottom panel. While the trend shown by the de-excitation processes from $j_1 = 5$ is similar to those already noted in Fig. 17, the processes from $j_1 = 10$ and 15 show, however, some differences. As an example, the transition from $j_1 = 10$ to $j_1' = 9$ involves an energy gap of $20B_e$, markedly larger than the one of $2B_e$ for the transition from $j_1 = 1$ to $j_1' = 0$. As a consequence, we find that the value of the related k is significantly lower for the de-excitation from $j_1 = 10$ to $j_1' = 9$ than it is for the $j_1 = 1$ to $j_1' = 0$ transition. The trend is even more marked when we examine de-excitations from $j_1' = 15$ in the bottom panel of Fig. 18. Such differences clearly confirm the important role played in the dynamics by energy gaps and the marked changes caused between transitions by the large density of states present in this anion.

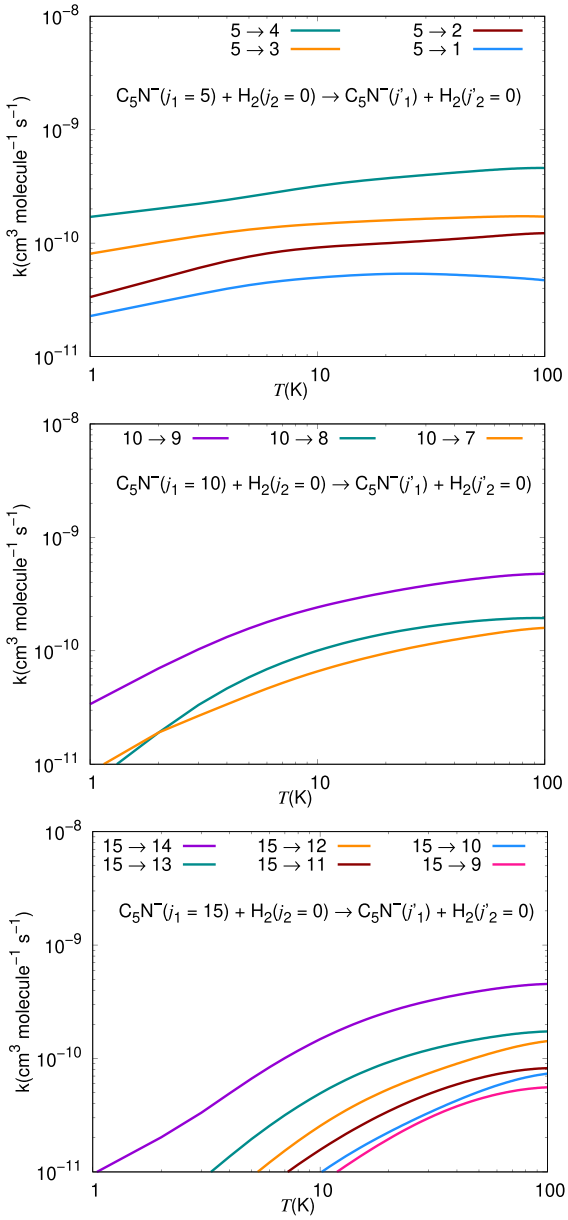

Figure 18. Computed rate coefficients k as a function of T for the de-excitation processes initiated from $j_1 = 5$ (top panel), 10 (middle panel), and 15 (bottom panel) to different j_1' states of C_5N^- in collision with H_2($j_2 = 0$).

3.1 Comparing C_5N^- rate coefficients from collisions with He and with $H_2(j_2 = 0)$

C_5N^- and C_3N^- (Lara-Moreno et al. 2017b, 2019a,b) correspond to two of the largest anions detected in the ISM. Thus, it would be interesting to compare their relative features when colliding with two common species in that environment: He and $H_2(j_2 = 0)$.

We first analyse in this Subsection the quantum dynamics of the larger anion with He and with $H_2(j_2 = 0)$, obtained in this study. The excitation cross-sections are reported in Fig. 19. They rise from their threshold in the two cases, and we see that the molecular partner uniformly yields larger inelastic cross-sections than the atomic one, as expected from the differences in strength of their two PESs discussed earlier in this paper. The cross-sections for the $j_1 = 0$

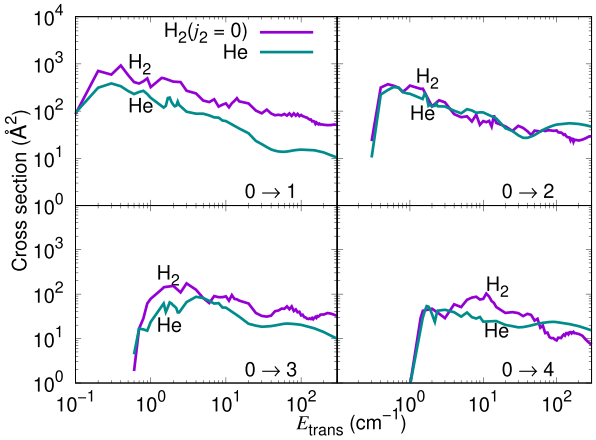

Figure 19. Excitation cross-section plotted as a function of $E_{\rm trans}$ for $j_1 = 0 \rightarrow j_1' = 1$, 2, 3, and 4 transitions in C_5N^- in collision with He and $H_2(j_2 = 0)$. The colour code of the processes is as follows: green for the former partner and purple for the latter one.

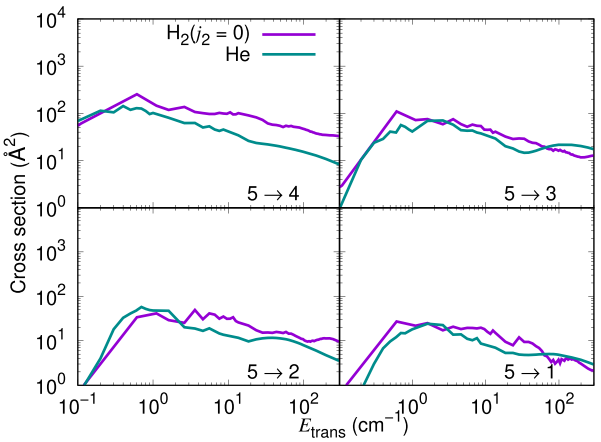

Figure 20. De-excitation cross-section plotted as a function of $E_{\rm trans}$ for $j_1 = 5 \rightarrow j_1' = 1$, 2, 3, and 4 transitions in C_5N^- in collision with He and $H_2(j_2 = 0)$. The colour code is the same as that in Fig. 19.

$\rightarrow j_1' = 1$ transition remain the larger in size over the energy range investigated and, on the whole, we can therefore state that H_2 is more effective in inducing state-changing transitions in the title molecule.

The comparison for de-excitation cross-sections, starting from the ($j_1 = 5$) initial state, is shown in Fig. 20. The general trends are very similar for both neutral projectiles, with a larger efficiency again obtained with the molecular collision partner. Although we see that the cross-sections for $\Delta j_1 = -1$ transitions are larger for H_2 than for He over the energy range investigated, the cross-section for $\Delta j_1' = -2$, -3, and -4 show smaller differences in size between the two types of cross-sections.Once more, our present calculations show that the cooling processes are more efficient when H_2 is the collision partner of C_5N^-.

When we now look in Fig. 21 at the corresponding inelastic rate coefficients, we clearly see that their computed values are uniformly and consistently larger for H_2 than He, in keeping with the cross-section behaviour of Fig. 19.

The de-excitation rate coefficients for the $j_1 = 5 \rightarrow j_1' = 1$, 2, 3, and 4 transitions are compared in the panels of Fig. 22. They

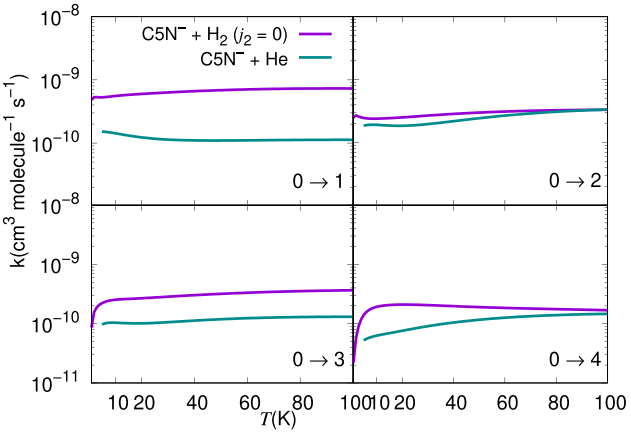

Figure 21. Plots of k versus T for several rotational excitation processes in $C_5N^-(j_1 = 0)$, comparing rate coefficients for He and $H_2(j_2 = 0)$.

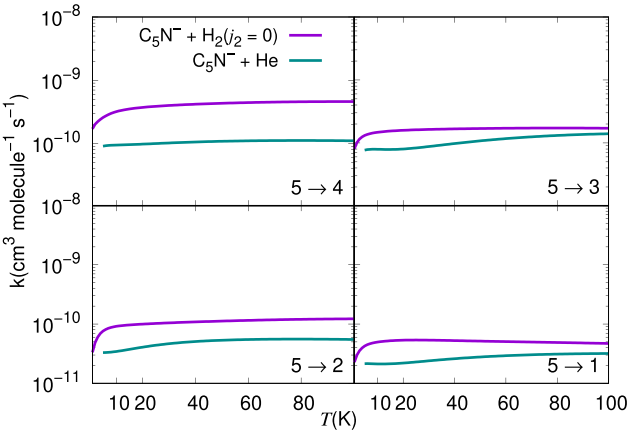

Figure 22. Plots of k versus T for several rotational de-excitation processes that start in the initial $C_5N^-(j_1 = 5)$ state. We compare the rate coefficients for He and $H_2(j_2 = 0)$ as partners.

again reflect the trends we have observed for the corresponding inelastic cross-sections: The k values are larger for collisions with H_2 and for $\Delta j_1 = -1$ transitions, while the $\Delta j_1 = -2$, -3, and -4 transitions show uniformly smaller rate coefficients and smaller differences between their sizes for the two neutral projectiles. This type of behaviour as a function of temperature is linked to the energy dependence shown earlier by the corresponding cross-sections reported in Figs 19 and 20.

A rather common procedure for neutral molecules has been to use the inelastic rate coefficients obtained from the He partner to approximate those expected for the H_2 partner by assuming that they can be taken to be the same cross-sections. Hence, the ensuing inelastic rate coefficients can be obtained as quantities scaled by the ratio of the reduced masses:

$$f1 = \frac{k_{\rm H_2}}{k_{\rm He}} = \sqrt{\frac{\mu_{\rm C_5N-He}}{\mu_{\rm C_5N-H_2}}} = 1.396. \quad (10)$$

For a relative scaling of He and H_2 partners in collision with molecular ions, a slightly more sophisticated scale factor can be used to additionally account for the differences between the ionic

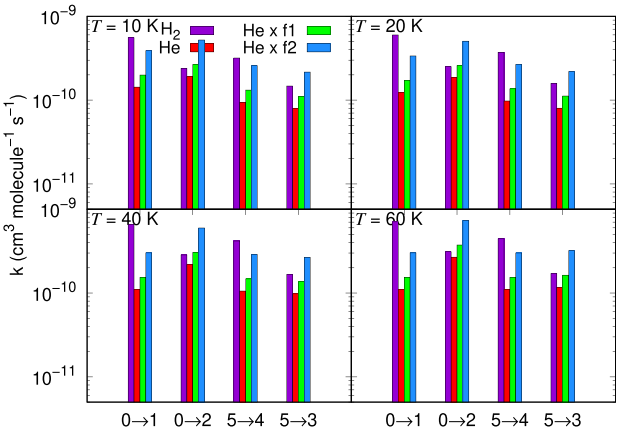

Figure 23. Comparison of rotationally inelastic rate coefficients for C_5N^- in collision with H_2 and with He. We also show those computed for the latter atom but scaled by the f1 and f2 factors discussed in the main text. The colour labelling is explained in the various panels.

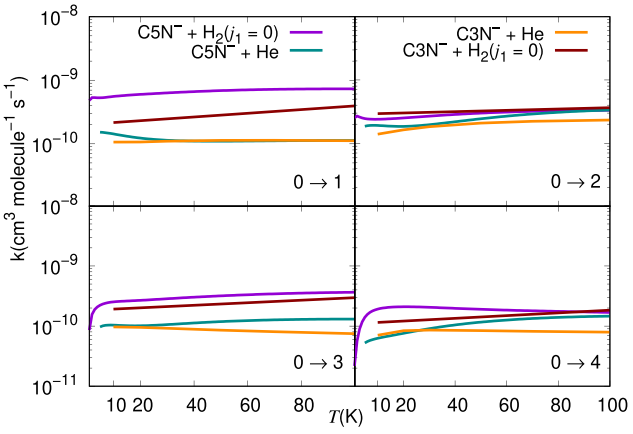

Figure 24. Computed excitation rate coefficients which compare C_5N^-, in collision with He and $H_2(j_2 = 0)$, with C_3N^- as obtained earlier in Lara-Moreno et al. (2017b, 2019b). The colour code for the various transitions is reported in the upper panels.

interactions:

$$f2 = \frac{k_{H_2}}{k_{He}} = \sqrt{\frac{\alpha^{st}(H_2)/\mu_{C_N-H_2}}{\alpha^{st}(He)/\mu_{C_N-He}}} = 2.73 \quad (11)$$

where $\alpha^{st}(He) = 1.384\ a_0^3$ and $\alpha^{st}(H_2) = 5.314\ a_0^3$ are the polarisabilities of He and H_2, respectively.

The specific validity of such scaling has been discussed in the literature rather extensively, e.g. via accurate calculations for the CO neutral target with different collision partners (Walker et al. 2014), and found to be unreliable. These authors therefore stressed the need to have the actual rate coefficients correctly computed for both partners to obtain more realistic data. In this study, we can therefore directly assess the validity of the scaling procedures by using our exact calculations for both projectiles as benchmark values in relation to the scaled results.

We therefore compare our correct rate coefficients for H_2 with those obtained from the He partner when scaling them with either of the above the factors. Our results are given in Fig. 23, which shows in its four panels the excitation rate coefficients for four different temperatures of interest. It is useful to note the following from the data in those panels:

(*i*) The exact results for He (red sticks) and H_2 (purple sticks) are seen to be different from each other at all temperatures and for all the four transitions considered. This is certainly in line with what we have discussed before.

(*ii*) The use of the *f1* scaling for the He results does not produce a realistic estimate of the correct inelastic rates for the H_2 partner: the green sticks in almost all the panels remain markedly smaller than the purple sticks pertaining to the correct calculations for the H_2 partner.

(*iii*) The use of the *f2* scaling formula seems to do more justice to reproducing the correct results for H_2. We see in the Figure that the blue sticks are yielding inelastic rates which are only slightly smaller than the correct ones (given by the purple sticks) for the $j_1 = 0 \rightarrow j_1' = 1$ transition. For all the other listed transitions, however, the scaled inelastic rates turn out to be generally larger than the correctly computed ones, especially for transitions between the higher rotational states.

In conclusion, we can say that, although the scaling suggested by equation (10) is providing better estimates of the inelastic rates with the H_2 partner, most of the scaled quantities are still different from those given by calculations which use the correct dynamics. The present test, therefore, indicates once more that, although the use of equation (10) provides a reasonable estimate of the correct rates for ionic systems, that scaling is still not sufficiently accurate to reliably replace the exact calculations.

3.2 Comparing C_5N^- and C_3N^- collisions with He and with $H_2(j_2 = 0)$

In this Subsection we compare the present calculations with those for the next smaller cyanopolyyne, i.e. the C_3N^- anion reported earlier by Lara-Moreno et al. (2017b, 2019a,b). These authors investigated excitation and de-excitation processes in a cyano-chain which has a much larger rotational constant ($B_e = 0.1618\ cm^{-1}$) than the one for C_5N^- ($0.046\,33\ cm^{-1}$). Thus, the rotational states of C_3N^- range from 0 to 30 and cross-sections were computed for E_{trans} from 0.1 to 2000 cm^{-1}, obtaining values for k in the range of 10–300 K. They found a dominance of the Δj_1 = even transitions over those with Δj_1 = odd transitions. In addition, they also found that de-excitation cross-sections summed over the final rotational states were comparable in magnitude to the Langevin cross-sections and decrease with $E_{trans}^{-0.5}$ increasing.

The panels given by Fig. 24 compare our findings with those obtained earlier for C_3N^-. We clearly see that the present results are consistently larger than those for the smaller anion. Further, we see that the rate coefficients for the $\Delta j_1 = 1$ transitions with the H_2 partner are the largest, while those with He are consistently smaller. Thus, the collisions with H_2 ($j_2 = 0$) yield the largest overall rates for the $\Delta j_1 = 1$ transitions and yield bigger rates than those for the He partner even for the larger Δj_1 transitions. In any case, the excitation rate coefficients for the present anion are always the larger in comparison with those for the smaller C_3N^- ($j_1 = 0$). The previous authors, in particular, had found that their rate coefficients for rotational excitation processes in C_3N^- ($j_1 = 0$), H_2 ($j_2 = 0$) were of the order of (1–4) $\times\ 10^{-10}\ cm^3\ molecule^{-1}s^{-1}$, with k decreasing with an increase in j_1'. Our computed rates are always markedly larger than the values associated with the C_3N^- partner.

The comparison of the rate coefficients for the de-excitation processes in C_5N^- and C_3N^- is reported in the four panels of Fig. 25. We see again that the transitions with $\Delta j_1 = -1$ are by far the largest

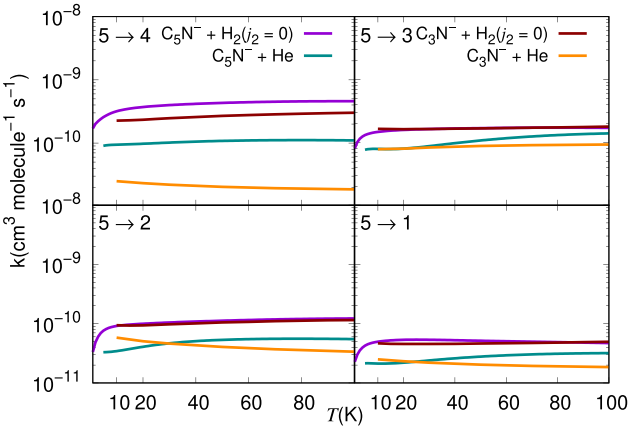

Figure 25. Computed de-excitation rate coefficients processes for C_5N^-, in collision with He and $H_2(j_2 = 0)$, and for C_3N^- as obtained earlier in Lara-Moreno et al. (2017b, 2019b).The colour code for the various transitions is reported in the upper panels.

for the case of the H_2 partner colliding with the larger anion, while for transitions with larger changes of the j_1 index the differences become less marked, albeit keeping the same general trend of yielding larger rates for the larger anion.

The data reported in the last two Figs 24 and 25 show that k values for $\Delta j_1 = +1$ and -1 exhibit in both systems similar behaviour in terms of temperature dependence, while however clearly showing that these excitation rates are larger for the C_5N^- than they are for the C_3N^-. Both sets of calculations also confirm that the H_2 partner is more efficient than He in causing rotational excitations and rotational cooling. For processes with Δj_1 varying through 1, 2, 3, 4, the partner H_2 remains more effective than He in causing excitations in C_5N^- and in C_3N^-, although the differences between the two anions become less marked for the larger Δj_1.

4 SUMMARY AND CONCLUSIONS

In this work, we have first obtained accurate ab initio PESs for the C_5N^- anion interacting with He and with H_2. For both systems the PESs were computed at the CCSD(T)-F12b/aug-cc-pVTZ level of theory, corrected for BSSE and extrapolated into the long-range region by using the analytic expressions of the leading interaction terms (see in earlier Sections). The validity of using the CCSD(T)-F12b procedure for these ionic interactions has been discussed many times in the literature and also analysed in our previous Section reporting the present ab initio data. An accurate ANN fit of the PES for the H_2 partner was carried out and also reported in detail in the present study. Both interactions were then expanded into multipolar coefficients that represent their anisotropic interactions via the correct angular functions for the 2D and the 4D systems (see earlier sections). Because of the large number of rotational states in this target, exact CC dynamical calculations were first carried out as a test of the quality of the HD reduction scheme, finding that for the present systems, the two coupling dynamics treatment are nearly equivalent at the considered energies. We have therefore resorted to using the HD dynamical approximation for the full calculations of the inelastic cross-sections of both systems, as described in detail in the previous Sections. The latter quantities were then used to obtain state-to-state inelastic rate coefficients as a function of T. In order to reliably extend the range of the computed rate coefficients up to 100 K, we have calculated the corresponding cross-sections, for all transitions, up to 300 cm^{-1}. The numerical quadrature hence yielded converged rate coefficient values within a few percentages.

Our present findings have shown that the state-to-state integral cross-sections for $j_1 = 0$ to $j_1' = 1$ are of the order of about 400 $Å^2$ for the He partner, and of about 1000 $Å^2$ for the H_2 partner, at the lowest energies tested in the calculations while slightly decreasing as collision energies increase. The cross-sections for excitation to j_1' = 2, 3, 4, and 5 exhibit a general increasing in size from threshold, reaching a maximum and then decreasing with increasing E_{trans}. The de-excitation cross-sections for $j_1 = 5$, when summed over $j_1' = 4$, 3, 2, and 1 turn out to be much smaller than the Langevin cross-sections, although also decreasing with increasing E_{trans} and showing large values at thresholds. The present calculations further confirm that the state-to-state rate coefficients for C_5N^-/H_2 are larger than those for the C_5N^-/He over the whole range of transitions examined. We further found that the integral cross-sections and rate coefficients for rotational transitions in C_5N^- were consistently larger than the corresponding results for C_3N^- (e.g. see Lara-Moreno et al. 2017b, 2019b). This is directly attributed to the larger anisotropy of the interacting PESs for C_5N^- and to its dramatically smaller rotational constant, when compared to the same features for C_3N^-, as we have discussed in detail in the previous section.

It is interesting to note at this point that the astronomical detection of the title molecular anion, together with that for the next smaller term in the series, C_3N^-, have been very recently achieved in the cold dark core TMC-1 of the Taurus region (Cernicharo et al. 2020), thus confirming the earlier findings in the circumstellar envelope of the carbon-rich star IRC +10216 more than ten years earlier. Although the formation mechanisms often suggested for the neutrals are different in interstellar (ion-neutral reactions) and circumstellar clouds (photodissociation and radical-neutral reactions), the similarity of the C_3N/C_3N^- and C_5N/C_5N^- abundance ratios found by the above detection study strongly suggests a common chemical path for the formation of these anions in interstellar and circumstellar clouds. Furthermore, detection of C_5N^- in TMC-1 gives strong support for assigning to this anion the lines found in IRC +10216, as it excludes the possibility of a metal-bearing species, or a vibrationally excited state. Hence, in the observational work of Cernicharo et al. (2020) new sets of rotational parameters have been derived from the observed frequencies in TMC-1 and IRC + 10216 for C_5N^-, in close similarity to the values used in this work (observed B_0 = 1388.866 81(19) MHz). A forest of rotational lines were observed, thereby suggesting that the anion was present in this cold dark core in a variety of rotational excited states.The collisional population of those excited states therefore becomes a realistic evolutionary path when we consider the rather large values of the rotational excitation rates found in this work, from collisions with He and with H_2 as partners. Since such partners are the most abundant neutral species both in envelopes and dark molecular clouds, we can therefore argue that even the detection in cold molecular cores can be made more possible by the existence of the large excitation paths exhibited by the present anion for collisions with neutral species like He and H_2, as was found from the calculations of this study. Such findings also indicate that these molecular anions are very likely to be in a non-LTE situation as far as their rotational state populations are concerned, although more specific kinetics modelling studies are still needed to confirm this suggestion. In any event, the collision paths to forming rotational excited states are found by the present calculations to be very effective energy-transfer mechanisms and therefore to be important reactions for modelling energy distributions within chemical kinetics studies involving these linear cyanopolyynes.

ACKNOWLEDGEMENTS

L.G.-S. and A.V. acknowledge the financial support by Ministerio de Ciencia, Innovación y Universidades (Spain). R.B. and U.L. thank NISER Bhubaneswar for providing computational facilities.

DATA AVAILABILITY

(i) Potential energy surface for the (C_5N^-–He) system provided as expansion multipolar coefficients as a function of (R, θ).

(ii) The FORTRAN subroutine for the C_5N^-–H_2 interaction potential obtained by the best ANN fit of the ab initio PES.

(iii) List of rotationally inelastic cross-section and rate coefficient values for the (C_5N^-–He) system.

(iv) List of rotationally inelastic cross-section and rate coefficient values for the (C_5N^-–H_2) system.

REFERENCES

Agúndez M., Cernicharo J., Guélin M., Gerin M., McCarthy M. C., Thaddeus P., 2008, A&A, 478, L19
Agúndez M. et al., 2010, A&A, 517, L2
Biswas R., Rashmi R., Lourderaj U., 2020, Resonance, 25, 59
Botschwina P., Oswald R., 2008, J. Chem. Phys., 129, 044305
Boys S., Bernardi F., 1970, Mol. Phys., 19, 553
Brünken S., Gupta H., Gottlieb C., McCarthy M., Thaddeus P., 2007, ApJ, 664, L43
Buonomo E., Gianturco F. A., de Lara-Castells M. P., Delgado-Barrio G., Miret-Artés S., Villarreal P., 1997, J. Chem. Phys., 106, 1718
Cernicharo J., Guélin M., Agúndez M., Kawaguchi K., McCarthy M., Thaddeus P., 2007, A&A, 467, L37
Cernicharo J., Marcelino N., Pardo J. R., Agúndez M., Tercero B., de Vicente P., Cabezas C., Bermúdez C., 2020, A&A, 641, L9
Cernicharo J., Guélin M., Agúndez M., McCarthy M. C., Thaddeus P., 2008, ApJ, 688, L83
Feller D., Peterson K., Grant Hill J., 2010, J. Chem. Phys., 133, 184102
Giri K., González-Sánchez L., Biswas R., Yurtsever E., Gianturco F. A., Sathyamurthy N., Lourderaj U., Wester R., 2022, J. Phys. Chem. A, 126, 2244
González-Sánchez L., Mant B. P., Wester R., Gianturco F. A., 2020, ApJ, 897, 75
Green S., 1975, J. Chem. Phys., 62, 2271
Hutson J. M., Sueur C. R. L., 2019a, MOLSCAT: A Program for Non-reactive Quantum Scattering Calculation on Atomic and Molecular Collisions
Hutson J. M., Sueur C. R. L., 2019b, Comput. Phys. Commun., 241, 9
Jerosimić S. V., Gianturco F. A., Wester R., 2018, Phys. Chem. Chem. Phys., 20, 5490
Kłos J., Lique F., 2011, MNRAS, 418, 271
Kolos W., Wolniewicz L., 1967, J. Chem. Phys., 46, 1426
Kouri D. J., 1975, Chem. Phys. Lett., 31, 599
Lara-Moreno M., Stoecklin T., Halvick P., 2017a, J. Chem. Phys., 146, 224310
Lara-Moreno M., Stoecklin T., Halvick P., 2017b, MNRAS, 467, 4174
Lara-Moreno M., Stoecklin T., Halvick P., 2019a, Phys. Chem. Chem. Phys., 21, 2929
Lara-Moreno M., Stoecklin T., Halvick P., 2019b, MNRAS, 486, 414
MATLAB, 2018, 9.5.0(R2018b). The MathWorks Inc., Natick, MA
MacKay D. J. C., 1992, Neural Comput., 4, 448
McCarthy M. C., Gottlieb C. A., Gupta H., Thaddeus P., 2006, ApJ, 652, L141
Raff L. M., Komanduri R., Hagan M., Bukkapatnam S. T. S., 2012, Neural Networks in Chemical Reaction Dynamics. Oxford Univ. Press, Oxford
Remijan A. J., Hollis J. M., Lovas F. J., Cordiner M. A., Millar T. J., Markwick-Kemper A. J., Jewell P. R., 2007, ApJ, 664, L47
Sarkar K., Bhattacharyya S. P., 2017, Soft-computing in Physical and Chemical Sciences: A Shift in Computing Paradigm. CRC Press, Boca Raton, Fl., USA
Sathyamurthy N., Raff L., 1975, J. Chem. Phys., 63, 464
Satta M., Gianturco F. A., Carelli F., Wester R., 2015, ApJ, 799, 228
Thaddeus P., Gottlieb C. A., Gupta H., Brünken S., McCarthy M. C., Agúndez M., Guélin M., Cernicharo J., 2008, ApJ, 677, 1132
Walker K., Yang B., Stancil P., Balakrishnan N., Forrey R., 2014, ApJ, 790, 96
Werner H.-J., Knowles P. J., Knizia G., Manby F. R., Schütz M., 2012, WIREs Comput. Mol. Sci., 2, 242

SUPPORTING INFORMATION

Supplementary data are available at *MNRAS* online.

Please note: Oxford University Press is not responsible for the content or functionality of any supporting materials supplied by the authors. Any queries (other than missing material) should be directed to the corresponding author for the article.

This paper has been typeset from a TEX/LATEX file prepared by the author.